World Electric Vehicle Journal

MDPI

Article

Research on Composite Liquid Cooling Technology for the Thermal Management System of Power Batteries

Lin Zhu, Dianqi Li and Ziyao Wu *

School of Mechanical Engineering, Shenyang University of Technology, Shenyang 110870, China; zhulin@smail.sut.edu.cn (L.Z.)
* Correspondence: wzy-12929@sut.edu.cn

Abstract: A battery thermal management system is crucial for maintaining battery temperatures within an acceptable range with high uniformity. A new BTMS combining a liquid cooling plate and vapor chamber is proposed and experimentally validated for ternary lithium soft pack batteries. An orthogonal test optimizes the liquid-cooling plate's structure at a 2C discharge rate. With a vapor chamber, the battery's temperature consistency improves. Experiments show that, at a 2C discharge rate, with coolant and ambient temperatures at 25 °C, the battery's maximum temperature is 35.191 °C, and the temperature difference is 3.77 °C. This represents a 2.1% increase in average temperature, and a 4.9% decrease in temperature difference compared to a liquid-cooling plate alone. The results indicate that the combined liquid-cooling and vapor chamber enhance temperature consistency.

Keywords: lithium-ion battery; battery thermal management system; vapor chamber; liquid-cooling plate

Academic Editor: Peter Van den Bossche

Received: 20 December 2024
Revised: 27 January 2025
Accepted: 30 January 2025
Published: 2 February 2025

Citation: Zhu, L.; Li, D.; Wu, Z. Research on Composite Liquid Cooling Technology for the Thermal Management System of Power Batteries. *World Electr. Veh. J.* **2025**, *16*, 74. https://doi.org/10.3390/wevj16020074

1. Introduction

In the context of the carbon peak and carbon-neutral era, new energy vehicles instead of traditional fuel vehicles can widely alleviate the problems of fossil fuel shortages and environmental pollution. Lithium batteries are often used as power batteries for new energy vehicles due to their advantages, such as low self-discharge rate, no memory effect, and high energy density [1].

In the process of charging and discharging, lithium batteries generate a large amount of heat, which is prone to leading to the thermal runaway phenomenon in the monomers inside the battery module, resulting in a serious imbalance in the temperature distribution between the individual monomers and localized overheating of the battery packs, which results in a mismatch in the performance of monomers between batteries, and further leads to premature failure of the battery module. Therefore, it is necessary to control the thermal behavior of the battery. Studies have shown that lithium-ion batteries must operate within a strict temperature paradigm range (20–55 °C), and operating outside of this temperature range can cause serious problems for the battery. The optimal operating range temperature is 20–40 °C. In addition, the temperature difference between all batteries should not exceed 5 °C [2,3]. A good Battery Thermal Management System (BTMS) improves the safety and life of the power battery, thus optimizing the performance and range of the vehicle.

According to the different cooling media, the battery thermal management system can be categorized into air cooling [4], liquid cooling [5], phase-change material cooling [6], heat pipe cooling [7], and composite cooling [8].

Liquid cooling (Minichannel Cold Plate, MCP) utilizes the liquid flow, which can quickly control the battery temperature, and utilizes the rapid heat dissipation of the liquid cooling plate to rapidly dissipate the heat generated by the battery into the environment [9]. However, the temperature difference between the inlet and outlet parts of its liquid cooling plate is large. Jia [10] analyzed that the number of pipes had the most significant effect on the average temperature of the liquid-cooling plate, and the pipe height had the least effect. In terms of temperature uniformity, the effects of the number of pipes and coolant flow rate were similar, and both were major influences, and the effects of pipe width and pipe height were similar, and both were minor influences. He [11] designed a double-layer I-shaped liquid cooling plate. Compared to the serpentine channel, this I-shaped liquid cooling plate can reduce the maximum temperature from 307.02 K to 303.94 K and the standard deviation of the surface temperature from 0.80 K to 0.25 K. Therefore, the I-shaped liquid cooling plate is a good solution to the problem.

The heat pipe-based BTMSs has a simple structure and better temperature uniformity. A vapor chamber (VC), which belongs to the heat pipe family, has a more extensive heat transfer area compared to the traditional heat pipe. Thanks to this, it is capable of achieving heat transfer in a two-dimensional plane, thus offering enhanced heat transfer performance and better temperature uniformity [12]. Xu [13] investigated the thermal control effect of S-shaped and U-shaped horizontal wave tubes. They found that the S-shaped tube showed higher cooling capacity, and the maximum temperature difference was reduced by 7.49%. The parallel design allows for a more uniform temperature distribution and lower pressure drop.

At present, it is difficult for a single cooling method to meet the demand of battery pack heat dissipation, and the composite cooling method can synthesize the advantages of a single cooling method, which is the research hotspot of power battery technology [14]. Zhao [15] proposed a phase change material (PCM)/microchannel coupled battery thermal management system (BTMS). Compared with liquid-cooled plates, the maximum temperature of the battery increased by 0.2 °C. However, the maximum temperature difference and pressure drop were reduced by 9.3% and 93.7%, respectively, and the volume of the optimized design decreased by 15.6%. Jang [16] proposed a novel BTMS that combines liquid cooling with a heat pipe. Compared with the liquid-cooled battery module, the maximum temperature of the B-type heat pipe liquid-cooled battery module was reduced by 6.1 °C. Wang [17] arranged the evaporation section of the L-shaped heat pipe between the square cells and the condensation section in the cooling runners at the bottom of the battery module.

However, the heat transfer performance of the heat pipe is also affected by the temperature rise along the coolant, and the heat pipe has a stronger heat transfer capability near the inlet of the coolant and a poorer heat transfer capability near the outlet of the coolant, which will result in the battery module still having a more pronounced temperature difference in the coolant flow direction.

The composite cooling system (Minichannel Cold Plate-Vapor Chamber, MCP-VC), which is based on the characteristics of the liquid cooling and the equalization plate cooling methods, makes the battery temperature more uniform while controlling the maximum battery temperature. In order to further study and optimize the cooling system of the power battery pack and improve the battery's homogeneous temperature, based on this, this paper firstly carries out the study of the cooling effect of the liquid cooling plate and analyzes the influence of each design parameter on the heat dissipation, and then uses the liquid cooling plate-mean temperature plate scheme for the power battery heat dissipation, and designs the composite heat dissipation system of the lithium battery.

2. Modeling of Lithium Battery

2.1. Physical Models

In this paper, the ternary lithium soft pack battery is the object of study, and the basic parameters of the battery are shown in Table 1.

Table 1. Lithium battery parameters.

Parameter	Parameter Value
Size/mm	167 × 164 × 10
Nominal capacity/Ah	46
Thermal conductivity/W/(m × K)	$\lambda_x = \lambda_y = 22.3$; $\lambda_z = 0.66$
Specific heat capacity/J/(kg × K)	1080
Density/kg/m^3	1933
Cathode materials	NCM
Anode materials	Graphite
Charge cut-off voltage/V	4.2
Discharge cut-off voltage/V	2.75

2.2. Thermal Model

This work uses Bernardi's battery heat generation rate model [18]. The following formula represents the rate of heat production (q) per unit volume of the battery:

$$q = \frac{I}{V_B}\left[(U - U_0) + T_B\frac{dU_0}{dT_B}\right] = \frac{I}{V_B}\left[IR + T_B\frac{dU_0}{dT_B}\right] \quad (1)$$

V_B is the battery's volume (m^3); I is its current, which is positive while charging and negative during discharging; R is the resistance, T_B is the battery's temperature, U is the open-circuit voltage, U_0 is the battery's terminal voltage, and $\frac{dU_0}{dT}$ is a constant of the voltage variation with temperature.

2.3. Battery Resistance Test Experiment

We tested Belt's proposed Hybrid Pulse Power Characteristic (HPPC), and collected voltage data at an ambient temperature of 25 °C. The following experimental steps were performed:

(1) We set the thermostat to 25 °C, charged the battery to full charge state (SOC = 1.0) using constant current and constant voltage, and then allowed it to cool to room temperature.

(2) We sequentially discharged the battery at 1C times constant current to a State of Charge (SOC) of 0.9, 0.8, 0.7, 0.6, 0.5, 0.4, 0.3, 0.2, and 0.1. At each interval, we let the battery rest for 30 min, and recorded the relevant current and voltage data.

Figure 1 shows the battery operating voltage profile at SOC = 90% during HPPC. The total internal resistance (R) of the battery corresponding to each SOC can be obtained from the experimental data.

The internal resistance of the battery is calculated as shown in Equations (2)–(4):

$$R_{ohm} = \frac{U1 - U2}{I} \quad (2)$$

$$R_{pot} = \frac{U2 - U3}{I} \quad (3)$$

$$R = R_{ohm} + R_{pot} \quad (4)$$

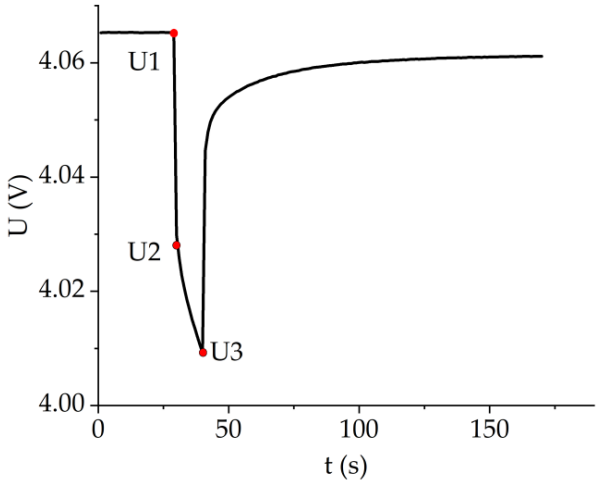

Figure 1. SOC = 90% discharge pulse local voltage profile.

Combining Equations (2)–(4), the relationship between R and SOC is obtained by fitting a fourth degree polynomial, as shown in Equation (5),

$$R = 0.00272 - 0.00559SOC + 0.00954SOC^2 - 0.0059SOC^3 - 0.000255342SOC^4 \quad (5)$$

In turn, the heat generation rate of the lithium battery is calculated to write UDF, which is simulated by FLUENT in this paper.

3. Composite Liquid-Cooling BTMS Design

3.1. Liquid Cooling Plate Heat Transfer Principle

According to the basic method of heat transfer, it can be seen that the liquid-cooling plate heat transfer mainly relies on heat conduction and heat convection [19]. The heat transfer path is that the battery heat is transferred to the liquid-cooling plate, and the coolant flow in the plate takes away the heat. Among them, heat conduction follows Fourier's law of thermal conductivity, which is calculated as

$$\Phi = -\lambda A \frac{dT}{dx} \quad (6)$$

where Φ is for the thermal conductivity, λ is for the thermal conductivity of the liquid-cooling plate, A is for the contact area, T is for the temperature, and x is for the thermal distance. According to Formula (6), it can be seen that the liquid cooling plate in the design of the material should be selected with high thermal conductivity and, combined with the economical, currently widely used aluminum liquid cooling plate, where the plate thickness is not easily too large, the liquid cooling plate and the battery contact area are as large as possible.

The energy equation of the battery is shown in Equation (7) [20],

$$\rho_B C_{p,B} \frac{\partial T_B}{\partial_t} = \nabla(k_B \nabla T_B) + q \quad (7)$$

where ρ_B is the density of the cell, $C_{p,B}$ is the specific heat capacity of the cell, and k_B is the thermal conductivity of the cell.

The coolant momentum, mass, and energy conservation equations are

$$\rho_w \left(\frac{\partial \vec{v}}{\partial t} + \vec{v} \cdot \nabla \vec{v} \right) = -\nabla P + \mu_w \nabla^2 \vec{v} \quad (8)$$

$$\frac{\partial \rho_w}{\partial t} + \nabla \cdot \left(\rho_w \vec{v}\right) = 0 \tag{9}$$

$$\rho_w C_{p,w} \frac{\partial T_w}{\partial t} + \nabla \cdot \left(\rho_w C_{p,w} \vec{v} \nabla T_w\right) = \nabla \cdot (\lambda_w \nabla T_w) \tag{10}$$

where ρ_w is the coolant density, t is the time, $\vec{v}$ is the coolant velocity vector, μ is the coolant dynamic viscosity, T_w is the coolant temperature, p is the coolant pressure, $C_{p,w}$ is the specific heat capacity of the coolant, and λ_w is the coefficient of thermal conductivity of the liquid cooling plate.

The Reynolds equation is

$$Re = \frac{\rho_w v d}{G} \tag{11}$$

where Re is the Reynolds number, V is the coolant flow velocity, G is the viscosity of the coolant, and d is the equivalent diameter of the channel. In this paper, the coolant velocity is selected to be 0.04 m/s, and the calculated Re is 1333, which is less than 2300, so it can be judged that the flow state of the coolant is laminar flow [21].

3.2. Liquid Cooling Plate Design

Before running numerical simulations, simplify the heat dissipation simulation model by assuming the following:

(1) The liquid-cooling plate is homogeneous and isotropic.
(2) The thermal conductivity of the liquid-cooling plate and the surface of the battery for convective heat transfer with air is 10 W/(m × K).
(3) The fluid is incompressible and stable, and the dynamic viscosity, specific heat capacity, and thermal conductivity are constant.
(4) The thermal material properties of fluids and solids are independent of temperature.

Here are the initial model boundary conditions:

(1) The inlet boundary condition is the velocity inlet boundary condition. We assume a uniform inlet velocity of the coolant and an inlet temperature of 25 °C.
(2) The outlet boundary condition suppresses backflow at the outlet end, as it is a pressure boundary condition. Since the fluid is incompressible and its nature is constant, only the relative value of pressure can be considered.

The heat generated by the battery is transferred to the top of the equalization plate through the contact surface of the equalization plate, and the liquid cooling plate is placed on the top of the equalization plate, arranged as shown in Figure 2. the external dimensions of the liquid cooling plate are the same as that of the battery, with a wall thickness of 4 mm, and the cooling medium is selected as liquid water.

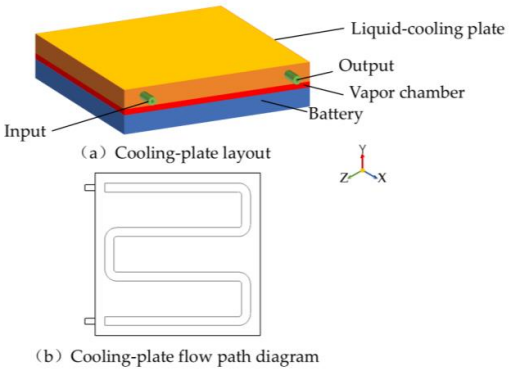

Figure 2. Schematics of battery thermal management systems: (**a**) cooling-plate layout; (**b**) cooling-plate flow path diagram.

3.3. Orthogonal Experiment

There are many factors that affect the cooling effect of the liquid cooling plate; in this paper, we will focus on four: the width of the cooling channel (A), the height of the cooling channel (B), the number of the cooling channel (C), and the coolant velocity (D). We take four different level values within reasonable limits for each factor, and the optimization aims to reduce the system temperature and temperature difference. Therefore, we chose the average temperature and temperature difference of the liquid-cooling plate as the indexes for this orthogonal experimental design. Because there are four degrees of freedom in the problem, and the factors interact in complex ways, it takes a lot of experiments to find the best set of parameters. A four-level, four-factor orthogonal table was designed as shown in Table 2. As shown in Table 2, each row represents a set of parameter structures of liquid-cooling plates, and 16 models are built according to the different parameter structures in each row.

Table 2. Orthogonal factor and level table.

Level	Factor			
	A (mm)	B (mm)	C	D (m/s)
1	9	5	4	0.01
2	11	6	5	0.02
3	13	7	6	0.03
4	15	8	7	0.04

3.4. Grid Independence

The structures for the battery thermal management system are more regular, so the quadrilateral and hexahedral structured grids are used for the whole model. In order to investigate the grid independency of simulation results, grids with 149,386, 195,384, 236,268, 268,581, 331,015, 405,189, 470,508 and 510,256 elements, respectively, are generated for the cooling channel model, which is tested in FLUENT.

It is found that the deviations of the average temperature, temperature difference, and channel pressure drop of the last three are all less than 1%. It can be concluded that the results of the last three grid cells are independent of the number of grids. Therefore, considering the solution accuracy and less convergence time, the sixth type of grid cell is selected for numerical research. The grid-independent results are shown in Figure 3.

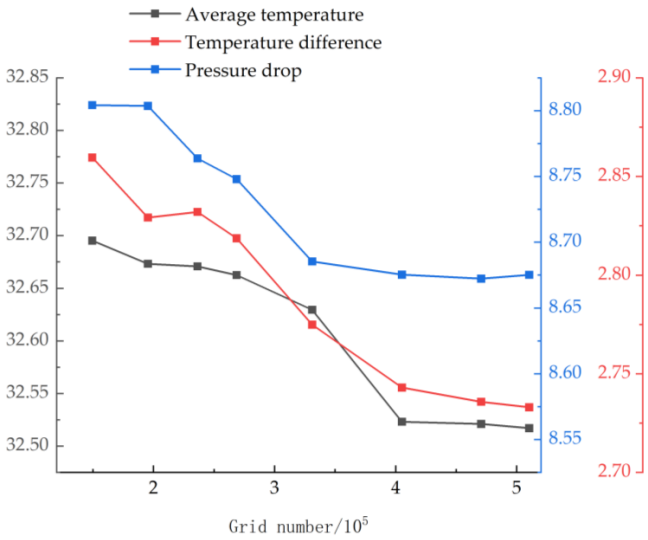

Figure 3. Grid independent results.

3.5. Orthogonal Experimental Scheme and Analysis

16 test models were simulated, and the data of the results were analyzed and sorted. Then T_{ave} and ΔT_{max} of the battery for each example are calculated, as shown in Table 3.

Table 3. Orthogonal design table results.

Number	Factor				Evaluation Index		
	A	B	C	D	T_{ave} (°C)	ΔT_{max} (°C)	ΔP (pa)
1	9	5	4	0.01	35.60	2.44	3.07
2	9	6	5	0.02	33.74	2.91	5.72
3	9	7	6	0.03	32.52	2.73	8.70
4	9	8	7	0.04	31.92	2.70	10.84
5	11	5	7	0.02	33.78	2.74	7.56
6	11	6	6	0.01	35.33	2.63	2.21
7	11	7	5	0.04	31.94	2.78	8.99
8	11	8	4	0.03	32.62	2.56	5.10
9	13	5	5	0.03	32.67	2.81	8.55
10	13	6	4	0.04	31.98	2.68	8.63
11	13	7	7	0.01	35.07	2.46	1.64
12	13	8	6	0.02	33.54	2.80	3.08
13	15	5	6	0.04	31.98	2.78	11.55
14	15	6	7	0.03	32.60	2.90	6.73
15	15	7	4	0.02	33.65	2.78	2.84
16	15	8	5	0.01	34.97	2.54	1.18

Levels can be selected on the basis of kinship. The greater the R_i, the greater the influence of the factor on the evaluation indicator. The correlation formula for R_i is as follows:

$$k_{in} = K_{mn}/4 \tag{12}$$

$$R_i = \max(k_{in}) - \min(k_{in}) \tag{13}$$

where i is 1, 2, 3, 4, representing factors A, B, C, and D, respectively; n is 1, 2, 3, and 4, representing four levels, respectively. m is 1 and 2, representing the indicators ΔT_{ave} and ΔT_{max}, respectively. k_{mn} denotes the sum of the evaluation indicators of factor i at n levels.

The impact of the level on the evaluation indicators can be judged directly from the value of the standard deviation (S_i), making the importance of the factor quantifiable. The formula is shown in the following equation:

$$S_i = \sqrt{\frac{\sum_{n=1}^{4}\left(k_{in} - \frac{1}{4}\sum_{n=1}^{4} k_{in}\right)}{4}} \tag{14}$$

The effects of four factors, A, B, C, and D, on the mean temperature and temperature difference were obtained by polar analysis as shown in Figures 4 and 5.

As shown in Table 4, for the average temperature, the R_i and S_i of factor D are the largest, and the R_i and S_i of factor C are the smallest, so the influence of each factor on the average temperature is in the order of D > B > A > C. The optimal combination of factors for the average temperature index is width 15 mm, height 8 mm, number of rows 5, and the flow rate 0.04 m/s. The trend of the change in the average temperature under each factor is shown in Figure 2, and the trend is decreasing with the increase in the rank. From the overall trend, the average temperature showed a decreasing trend with the increase in

the grade. Therefore, factors A, B, and D can be maximized as far as the practical situation allows.

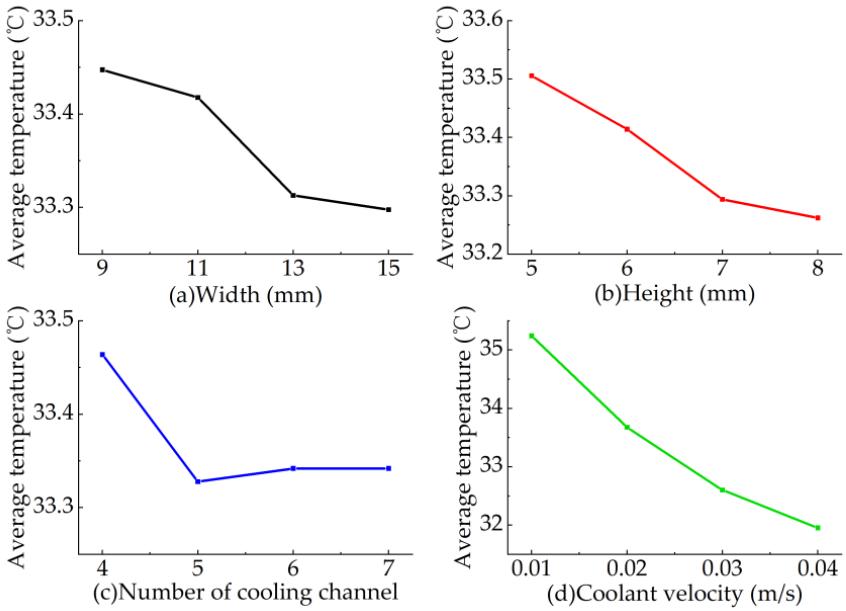

Figure 4. Trends in average temperature under the influence of various factors: (**a**) the width of the cooling channel; (**b**) the height of the cooling channel; (**c**) the number of the cooling channel; (**d**) the coolant velocity.

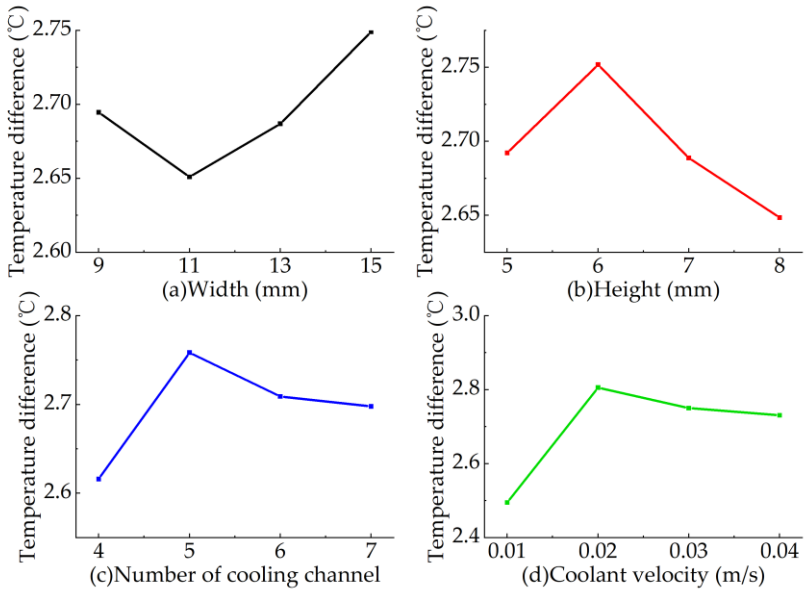

Figure 5. Trends in temperature difference under the influence of various factors: (**a**) the width of the cooling channel; (**b**) the height of the cooling channel; (**c**) the number of the cooling channel; (**d**) the coolant velocity.

For the temperature difference, the Ri and Si of factor D are the largest, and the Ri and Si of factor B are the smallest, so the influence of each factor on the temperature difference is in the order of D > C > A > B. The optimal combination under the index for the temperature difference is 11 mm in width, 8 mm in height, four rows, and a flow rate of 0.01 m/s. The trend of the temperature difference under the factors is shown in Figure 5. It can be seen that with the increase in the level, factor B and factor D generally show the trend of increasing first and then decreasing. When the channel height is 8 mm, factor B minimizes

the temperature difference. For factor D, the temperature difference is the smallest when the coolant flow rate is 0.1 m/s, but the average temperature is the largest at this time. We should follow preference when selecting the optimal level for factor A based on the average temperature index. When factor C is selected as 5, 6, and 7, the difference in average temperature is not significant, but the temperature difference is the smallest when the number of runner rows is seven.

Table 4. Polar analysis of mean temperature and temperature difference.

Evaluation Index		Factor			
		A	B	C	D
ΔT_{max} (°C)	K_{11}	133.79	134.02	133.86	140.97
	K_{12}	133.67	133.66	133.31	134.71
	K_{13}	133.25	133.18	133.37	130.40
	K_{14}	133.19	133.05	133.37	127.82
	k_{i1}	33.45	33.51	33.46	35.24
	k_{i2}	33.42	33.41	33.33	33.68
	k_{i3}	33.31	33.29	33.34	32.60
	k_{i4}	33.30	33.26	33.34	31.95
	R_i	0.150	0.244	0.136	3.288
	S_i	0.065	0.097	0.055	1.245
T_{ave} (°C)	K_{12}	10.50	10.91	11.03	11.22
	K_{13}	10.75	10.76	10.74	11.00
	K_{14}	11.00	10.59	10.79	10.92
	k_{i1}	2.69	2.6922	2.62	2.47
	k_{i2}	2.63	2.7269	2.76	2.81
	k_{i3}	2.69	2.6888	2.68	2.75
	k_{i4}	2.75	2.6485	2.70	2.73
	R_i	0.123	0.078	0.142	0.336
	S_i	0.044	0.028	0.051	0.130

In summary, the optimal levels should be taken as A4, B4, C4, and D4.

3.6. Optimized Liquid-Cooling Plate Structure

As depicted in Figure 6, the orthogonal experiments reveal that the relatively optimal combination model 17, with dimensions of 15 mm in width and 8 mm in height, controls the average temperature at a lower level than the other 16 groups. When the model is 15 mm in width, 8 mm in height, has seven rows, and has a 0.04 m/s flow rate, the average temperature of the cell is 31.89 °C, and the temperature difference is 2.85 °C.

3.7. Composite Liquid-Cooling Structure

In this paper, a power battery thermal management scheme using a composite of a liquid-cooling plate and a Vapor chamber is proposed, and a Vapor chamber is arranged between the battery and the liquid-cooling plate, as shown in Figure 1 for model 18 (MCP-VC). The equivalent thermal conductivity of the Vapor chamber is 5000 W/(m × K).

The average temperature of model 18 is 32.42 °C, and the temperature difference is 1.40 °C. Compared with model 17 (MCP), the average temperature increases by 1.65%, and the temperature difference decreases by 50.83%.

The cell cross-section temperature distributions of the two cooling structures are presented in Figure 7, visually demonstrating the differences in temperature uniformity between the two cases.

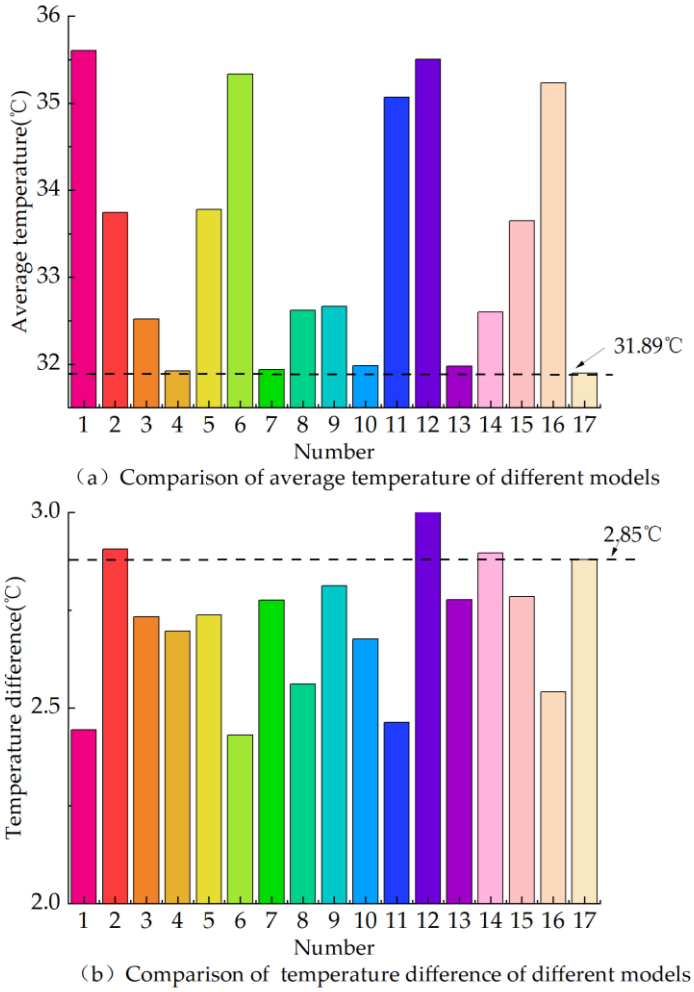

Figure 6. Comparison of different models: (**a**) comparison of average temperature for different models; (**b**) comparison of temperature difference for different models.

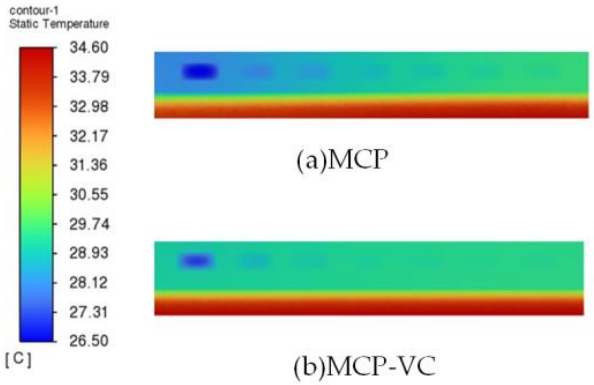

Figure 7. Temperature distribution of cross sections for different cooling structures: (**a**) MCP; (**b**) MCP-VC.

4. Experiment

4.1. Experimental Equipment

Experiment-related test equipment includes the Xinwei (China) CT-4004-5V100A-NFA charge/discharge system, Topray (China) TP700 temperature acquisition system, T-type thermocouples, Shanghai YIHE (China) scientific thermostatic box, Jieheng (China) KY-300EA peristaltic pump, upper computer, liquid-cooling plate, as well as the homogeneous

temperature plate. Figure 8 displays the schematic diagram of the experimental setup. The blue line depicts the coolant inflow, while the red line depicts the coolant outflow.

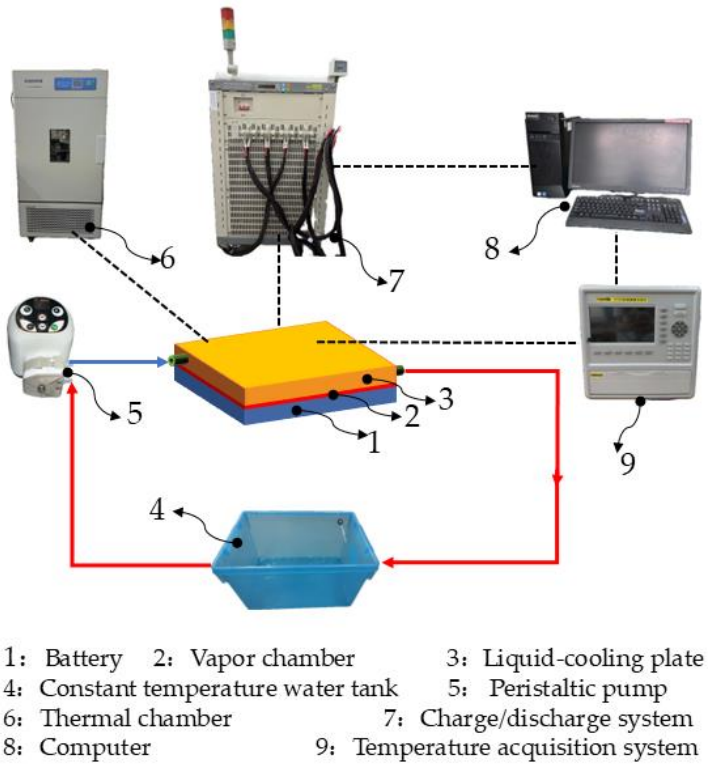

Figure 8. Experimental platform.

4.2. NC Experimental Validation

A battery tester was used to operate the soft pack lithium battery at a 2C discharge multiplication rate. The lithium battery was placed in a thermal chamber at 25 °C, and eight main temperature test points were arranged according to the heat generation-heat transfer mechanism and temperature distribution characteristics of the lithium-ion battery to reflect the overall temperature change in the battery. Test point locations: battery front negative end (test point 1), battery front positive end (test point 2), battery front center (test point 3), battery front center corresponding to the bottom (test point 4), battery back negative end (test point 5), battery back positive end (test point 6), battery back center (test point 7), and battery back center corresponding to the bottom (test point 8). The temperature data from the thermocouples were collected using the Topray TP700 temperature collector and transferred to the computer. The average temperature measured by the eight thermocouples was used as the experimental value, and the average value of the temperature on the middle surface of the battery was used as the simulation temperature value. Figure 9 demonstrates the comparison between the experimental and simulation results under natural convection (NC). As shown in Figure 9, the curves of simulation and experiment are in good agreement, and the maximum relative error is not more than 3.5%. When the battery is discharged at 2C multiplicity, the maximum average temperature of the battery exceeds 45 °C. Therefore, an efficient BTMS needs to be designed to reduce the battery temperature.

The simulation defines the battery as a solid heat source, and the temperature difference is tiny, at 0.76 °C in the NC simulation. In fact, the positive pole of the battery generates heat, so the highest point of the experimental temperature is point 6, and the lowest point of the temperature is point 8.

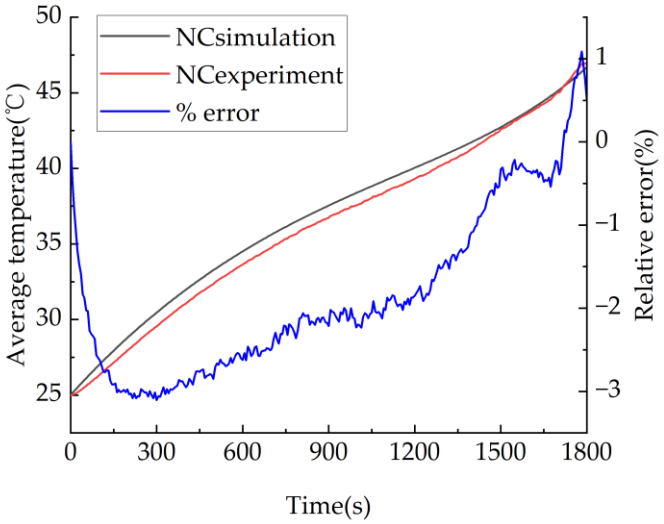

Figure 9. Comparison of NC experiment and simulation.

4.3. Experimental Validation of MPC and MCP-VC

We placed the cooling device in a thermal chamber at 25 °C. Figure 10 shows that the cooling device was covered with 1 mm of silicone grease that has a thermal conductivity of 2 W/(m × K) between the battery and the Vapor chamber to make it fit better. At a temperature of 25 °C, the coolant flow rate was 0.04 m/s.

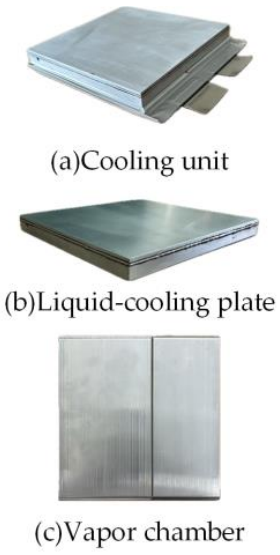

Figure 10. Performance of MCP-VC cooling and physical drawing of the device: (**a**) cooling unit; (**b**) liquid-cooling plate; (**c**) vapor chamber.

The simulation and experimental results are shown in Figure 11; the average temperature of the MCP experiment is 35.95 °C, and the maximum temperature difference is 3.98 °C; the average temperature of the MCP-VC experiment is 35.13 °C, and the maximum temperature difference is 3.69 °C. The average temperature decreased by 2.3%, and the temperature difference decreased by 7.2%, with the same trend as the simulation results. The experimental temperatures are all higher than the simulation temperature, presumed to be the incomplete fitting between the structures and the presence of air with low thermal conductivity, which affects the cooling effect.

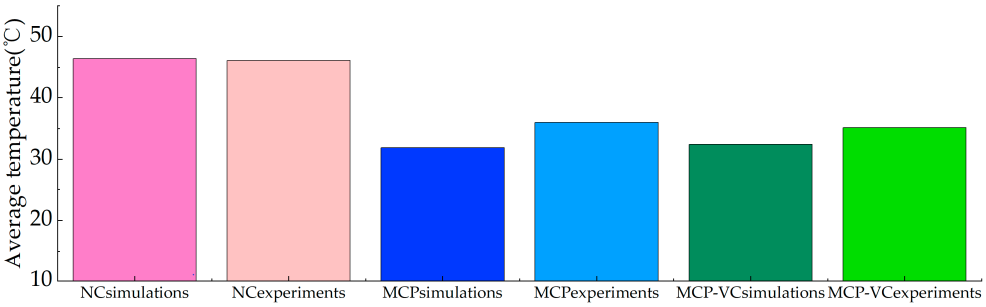

(a)Effect of different cooling methods on the average temperature

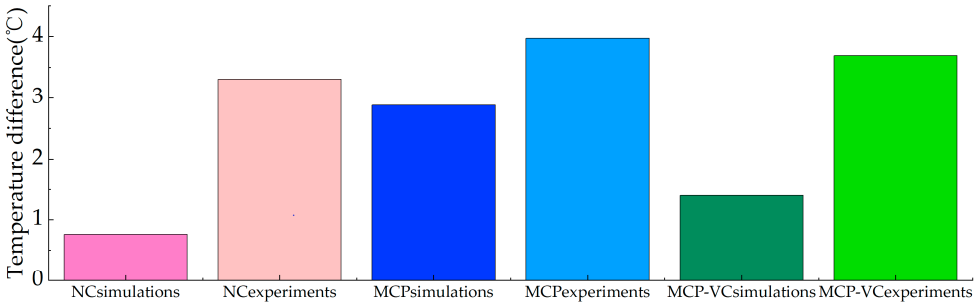

(b)Effect of different cooling methods on the temperature difference

Figure 11. Effect of different cooling methods on average temperature and temperature difference: (**a**) average temperature; (**b**) temperature difference.

4.4. Experimental Validation of MCP-VC at Different Coolant Speeds

In both modes of MCP cooling and MCP-VC cooling, the average temperature decreases with increasing coolant velocity, and the temperature difference increases with increasing coolant velocity. Figure 12 displays that the average temperature dropped by 10% when the speed of the coolant was raised from 0.01 m/s to 0.04 m/s in the experimental case. The average temperature of MCP-VC was lower than that of the MCP mode at any coolant velocity. The temperature differences between the MCP-VC mode and the MCP mode at coolant velocities of 0.01 m/s, 0.02 m/s, 0.03 m/s, and 0.04 m/s were significantly different from the slow rise in temperature difference in the MCP mode. This was because the lowest point of the cells' temperatures changed. For the first two groups, it was point 4, which is in the middle of the cell's frontal side and corresponds to the bottom; for the third group, it was point 1, which is the cell front negative bottom.

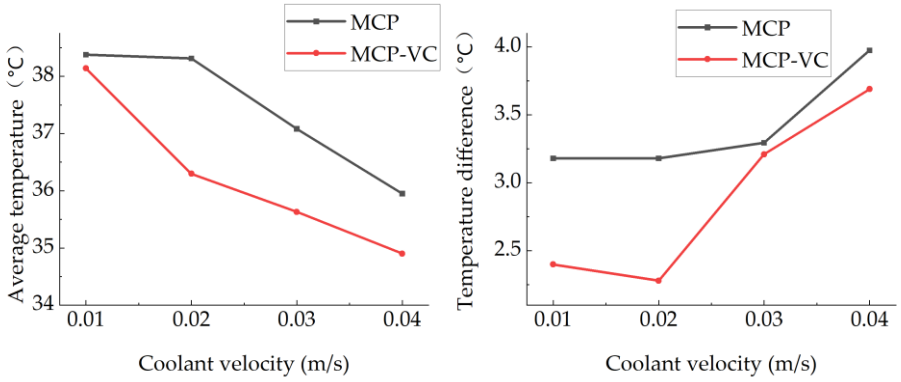

Figure 12. Effect of different coolant velocity on the average temperature and temperature difference at 2C discharge rates.

4.5. Low-Temperature Preheating Analysis

The model employed for the preheating simulation, which encompasses the liquid, the cooling plate, and the Vapor chamber, is identical to the numerical model utilized in

the cooling simulation. The ambient temperature is −10 °C. The coolant inlet temperatures are 15 °C, 20 °C, 25 °C, and 30 °C, and the flow rate is 0.04 m/s.

Numerical simulation results (Figure 13) demonstrate that the warm-up process decelerates as the coolant temperature drops. For batteries with coolant temperatures of 15 °C, 20 °C, 25 °C, and 30 °C, it takes 894 s, 651 s, 524 s, and 448 s, respectively, to heat the battery to 5 °C. The results suggest that increasing the coolant temperature enables the battery module to be pre-heated more rapidly.

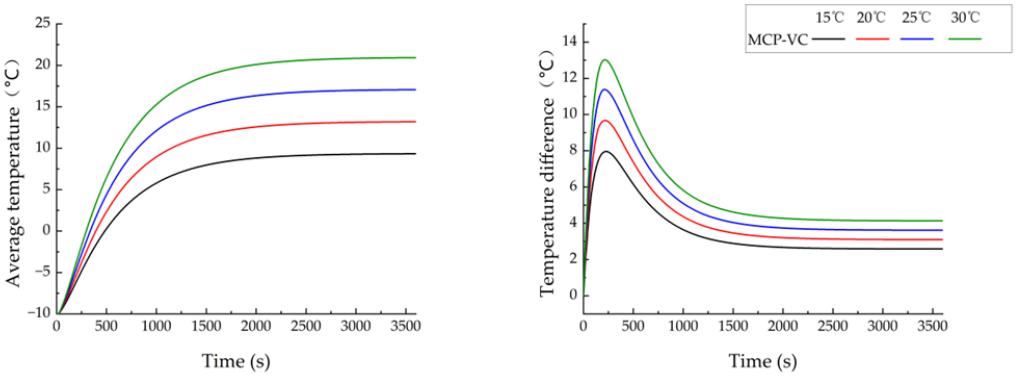

Figure 13. The curves of the average temperature, temperature difference and time of the battery at 5 °C, 15 °C, 25 °C, 30 °C and three inlet temperatures.

The temperature difference during the preheating process will first increase, then decrease, and finally stabilize. When the inlet temperatures of the heating medium are 15 °C, 20 °C, 25 °C, and 30 °C, the times required for the MCP-VC to reduce the temperature difference to 5 °C during the preheating process are 669 s, 843 s, 1029 s, and 1269 s, respectively.

Elevating the temperature of the heating medium can significantly enhance the preheating capacity while shortening the preheating duration. However, a relatively high temperature of the heating medium leads to greater energy consumption and a longer time to meet the requirement for temperature uniformity.

5. Conclusions

There is a new BTMS with a liquid-cooling plate and a temperature equalization plate in this paper. It is meant to help the battery thermal management system transfer heat quickly and keep temperatures even. A three-dimensional numerical model is established, and parameters such as runner width, height, number of runners and coolant flow rate are optimized through orthogonal tests to effectively reduce the average temperature and temperature difference in the battery. Finally, an equalization plate was added between the battery and the liquid-cooling plate to further reduce the temperature difference. The thermal performance of the three BTMSs based on NC, MCP and MCP-VC is evaluated, and the main conclusions are as follows:

(1) The liquid-cooling plate has the best heat dissipation effect when the model is 15 mm in width, 8 mm in height, has seven rows, and has a 0.04 m/s flow rate. The average temperature of the battery under simulation is 31.89 °C, and the temperature difference is 2.85 °C; the average temperature of the battery under experiment is 34.41 °C, and the temperature difference is 3.88 °C.

(2) The addition of an equalization plate between the liquid-cooling plate and the battery further reduces the temperature difference. MCP cooling improves the temperature uniformity of the battery module compared with MCP-VC cooling. When the coolant comes in at 25 °C, MCP-VC cooling keeps the average temperature below 36 °C at

the end of the 2C discharge. The average temperature difference is 2.3% lower with MCP-VC cooling than with MCP cooling, and it is 7.2% smaller with MCP cooling than with MCP cooling.

(3) Increasing the coolant inlet velocity can effectively reduce the average temperature, and this effect is more significant for MCP-VC cooling than for MCP cooling. When the speed of the coolant inlet was raised from 0.01 m/s to 0.04 m/s at a 2C discharge multiplicity, the average temperature dropped by 10% under MCP-VC cooling. At any coolant velocity, the average temperature of MCP-VC was lower than that of MCP mode, and the temperature difference of MCP-VC was lower than that of MCP.

Author Contributions: Conceptualization, L.Z. and Z.W.; methodology, L.Z.; software, L.Z.; validation, L.Z.; formal analysis, L.Z.; investigation, L.Z.; resources, Z.W.; data curation, L.Z.; writing—original draft preparation, L.Z.; writing—review and editing, D.L.; supervision, D.L.; project administration, D.L. All authors have read and agreed to the published version of the manuscript.

Funding: This research received no external funding.

Data Availability Statement: The original contributions presented in the study are included in thearticle, further inquiries can be directed to the corresponding author.

Conflicts of Interest: The authors declare no conflict of interest.

Glossary

List of Abbreviations

BTMS	Battery Thermal Management System
NCM	Nickel Cobalt Manganese
SOC	State of Charge
HPPC	Hybrid Pulse Power Characteristic
NC	Natural Convection
MCP	Minichannel Cold Plate
MCP-VC	Minichannel Cold Plate-Vapor Chamber

List of Mathematical Symbols

V_B	Battery's volume, m^3
I	Current, A
R	Resistance, Ω
T_B	Battery's temperature, °C
U	Open-circuit voltage, V
U_0	battery's terminal voltage V
$\frac{dU_0}{dT}$	Constant of the voltage variation with temperature,
Φ	Thermal conductivity, W/(m × K)
λ	Thermal conductivity of the liquid-cooling plate, W/(m × K)
A	Contact area, m^2
x	Thermal distance, m
ρ_B	Density of the cell, kg/m^3
$C_{p,B}$	Specific heat capacity of the cell, J/(kg × K)
k_B	Thermal conductivity of the cell, W/(m × K)
ρ_w	Coolant density, kg/m^3
$\vec{v}$	Coolant velocity vector, m/s
M	Coolant dynamic viscosity, Pa·s
T_w	Coolant temperature, °C
P	Coolant pressure, Pa
$C_{p,w}$	Specific heat capacity of the coolant, J/(kg × K)
λ_w	Coefficient of thermal conductivity of the liquid cooling plate, W/(m × K)

Re	Reynolds number,
V	Coolant flow velocity, m/s
G	Viscosity of the coolant, Pa·s
d	Equivalent diameter of the channel, m

References

1. Tian, H.; Qin, P.; Li, K.; Zhao, Z. A review of the state of health for lithium-ion batteries: Research status and suggestions. *J. Clean Prod.* **2020**, *261*, 120813. [CrossRef]
2. Cheng, J.; Shuai, S.; Tang, Z.; Changfa, T. Thermal performance of a lithium-ion battery thermal management system with vapor chamber and minichannel cold plate. *Appl. Therm. Eng.* **2023**, *222*, 119694. [CrossRef]
3. Wang, D.; Xie, J. Investigation of the Liquid Cooling and Heating of a Lithium-Ion Battery Package for an Electric Vehicle. *World Electr. Veh. J.* **2023**, *14*, 169. [CrossRef]
4. Park, S.; Yu, J.K.; Lee, H.; Choi, H.K. Flow study on lithium-ion battery pack with air cooling. *J. Mech. Sci. Technol.* **2023**, *37*, 4631–4638. [CrossRef]
5. Li, B.; Mao, Z.; Song, B.; Lu, C.; Tian, W.; Zhang, B. Study on battery thermal management of autonomous underwater vehicle by bionic wave channels with liquid cooling. *Int. J. Energy Res.* **2021**, *45*, 13269–13283. [CrossRef]
6. Rohit Kumar, K.; Sharan, V.; Harish, R.; Shyam Kumar, M.B. Numerical study of thermal cooling for Lithium-ion battery pack using phase change material. *Iop Conf. Series. Earth Environ. Sci.* **2020**, *573*, 12018. [CrossRef]
7. Chung, W.; Lee, J.; Rhi, S. Thermal management system using pulsating heat pipe of cylindrical battery cell. *J. Mech. Sci. Technol.* **2023**, *37*, 6711–6725. [CrossRef]
8. Lin, J.; Liu, X.; Li, S.; Zhang, C.; Yang, S. A review on recent progress, challenges and perspective of battery thermal management system. *Int. J. Heat Mass Transf.* **2021**, *167*, 120834. [CrossRef]
9. Liang, J.; Gan, Y.; Li, Y. Investigation on the thermal performance of a battery thermal management system using heat pipe under different ambient temperatures. *Energy Conv. Manag.* **2018**, *155*, 1–9. [CrossRef]
10. E, J.; Han, D.; Qiu, A.; Zhu, H.; Deng, Y.; Chen, J.; Zhao, X.; Zuo, W.; Wang, H.; Chen, J.; et al. Orthogonal experimental design of liquid-cooling structure on the cooling effect of a liquid-cooled battery thermal management system. *Appl. Therm. Eng.* **2018**, *132*, 508–520. [CrossRef]
11. He, P.; Lu, H.; Fan, Y.; Ruan, H.; Wang, C.; Zhu, Y. Numerical investigation on a lithium-ion battery thermal management system utilizing a double-layered I-shaped channel liquid cooling plate exchanger. *Int. J. Therm. Sci.* **2023**, *187*, 108200. [CrossRef]
12. Zhao, J.; Jian, Q.; Huang, Z. Experimental study on heat transfer performance of vapor chambers with potential applications in thermal management of proton exchange membrane fuel cells. *Appl. Therm. Eng.* **2020**, *180*, 115847. [CrossRef]
13. Xu, H.; Zhang, X.; Xiang, G.; Li, H. Optimization of liquid cooling and heat dissipation system of lithium-ion battery packs of automobile. *Case Stud. Therm. Eng.* **2021**, *26*, 101012. [CrossRef]
14. Yue, Q.L.; He, C.X.; Wu, M.C.; Zhao, T.S. Advances in thermal management systems for next-generation power batteries. *Int. J. Heat Mass Transf.* **2021**, *181*, 121853. [CrossRef]
15. Zhao, D.; Chen, M.; Lv, Z.S.W. Multi-objective optimization of battery thermal management system combining response surface analysis and NSGA-II algorithm. *Energy Convers. Manag.* **2023**, *292*, 1. [CrossRef]
16. Jang, D.S.; Yun, S.; Hong, S.H.; Cho, W.; Kim, Y. Performance characteristics of a novel heat pipe-assisted liquid cooling system for the thermal management of lithium-ion batteries. *Energy Conv. Manag.* **2022**, *251*, 115001. [CrossRef]
17. Liu, W.; Jia, Z.; Luo, Y.; Xie, W.; Deng, T. Experimental investigation on thermal management of cylindrical Li-ion battery pack based on vapor chamber combined with fin structure. *Appl. Therm. Eng.* **2019**, *162*, 114272. [CrossRef]
18. Bernardi, D.; Pawlikowski, E.; Newman, J. A General Energy Balance for Battery Systems. *J. Electrochem. Soc.* **1985**, *132*, 5. [CrossRef]
19. Zhao, Y.; Chen, J.; He, W. Design and Performance Evaluation of Liquid-Cooled Heat Dissipation Structure for Lithium Battery Module. *Processes* **2023**, *11*, 1769. [CrossRef]
20. Shan, S.; Li, L.; Xu, Q.; Ling, L.; Xie, Y.; Wang, H.; Zheng, K.; Zhang, L.; Bei, S. Numerical investigation of a compact and lightweight thermal management system with axially mounted cooling tubes for cylindrical lithium-ion battery module. *Energy* **2023**, *274*, 127410. [CrossRef]
21. Zhao, D.; An, C.; Jia, Z.; Lei, Z. Structure optimization of liquid-cooled plate for electric vehicle lithium-ion power batteries. *Int. J. Therm. Sci.* **2024**, *195*, 108614. [CrossRef]